# Mass measurements of neutron-rich $A \approx 90$ nuclei constrain element abundances

W. Xian [1,2,*] S. Chen [1,2,†] S. Nikas [3] M. Rosenbusch [2] M. Wada [2] H. Ishiyama [4] D. Hou [5] S. Iimura [4]
S. Nishimura [4] P. Schury [2] A. Takamine [4] S. Yan [6] F. Browne [4] P. Doornenbal [4] F. Flavigny [7] Y. Hirayama [2]
Y. Ito [8] S. Kimura [4] T. M. Kojima [4] J. Lee [1] J. Liu [1] H. Miyatake [2] S. Michimasa [9] J. Y. Moon [10] S. Naimi [4]
T. Niwase [2,11,4] T. Sonoda [4] D. Suzuki [4] Y. X. Watanabe [2] V. Werner [12,13] K. Wimmer [14,15,4] and H. Wollnik [16]

[1]*Department of Physics, The University of Hong Kong, Pokfulam 999077, Hong Kong*
[2]*KEK Wako Nuclear Science Center, Wako, Saitama 351-0198, Japan*
[3]*Department of Physics, University of Jyväskylä, FI-40014 Jyväskylä, Finland*
[4]*RIKEN Nishina Center, Wako, Saitama 351-0198, Japan*
[5]*Institute of Modern Physics, Chinese Academy of Sciences, Lanzhou 730000, China*
[6]*Institute of Mass Spectrometry and Atmospheric Environment, Jinan University, Guangzhou 510632, China*
[7]*Université de Caen Normandie, ENSICAEN, CNRS/IN2P3, LPC Caen, UMR6534, F-14000 Caen, France*
[8]*Advanced Science Research Center, Japan Atomic Energy Agency, Ibaraki 319-1195, Japan*
[9]*Center of Nuclear Study (CNS), The University of Tokyo, Bunkyo 113-0033, Japan*
[10]*Institute for Basic Science, 70, Yuseong-daero 1689-gil, Yusung-gu, Daejeon 305-811, Korea*
[11]*Kyushu University, Hakozaki, Higashi-ku, Fukuoka 812-8581, Japan*
[12]*Institut für Kernphysik, Technische Universität Darmstadt, Darmstadt 64289, Germany*
[13]*Helmholtz Forschungsakademie Hessen für FAIR (HFHF), GSI Helmholtzzentrum für Schwerionenforschung,
Campus Darmstadt, 64289 Darmstadt, Germany*
[14]*Department of Physics, The University of Tokyo, 7-3-1 Hongo, Bunkyo, Tokyo 113-0033, Japan*
[15]*GSI Helmholtzzentrum für Schwerionenforschung, 64291 Darmstadt, Germany*
[16]*New Mexico State University, Las Cruces, New Mexico 88001, USA*

Atomic masses of the neutron-rich isotopes $^{83,84}$Ga, $^{82-86}$Ge, $^{82-89}$As, $^{82,84-91}$Se, $^{85,86,89-92}$Br, $^{89,91,92}$Kr, and $^{91}$Rb have been measured with high precision and accuracy using the multi-reflection time-of-flight mass spectrograph at the RIBF facility. The masses of $^{88,89}$As were measured for the first time and the mass uncertainties of $^{86}$Ge and $^{90,91}$Se were significantly reduced from several hundred keV to below the 10 keV scale. Investigation of shell evolution and potential subshell closures are proceeded by analysis of two-neutron separation energy systematics. As a result of the precise mass measurements, no prominent change on the slope of the two-neutron separation energy beyond $N = 56$ is observed in Se isotopes, indicating the subshell closure effect at $N = 56$ of Se does not exist. Also, various leading mass models are compared with the measurements. The impact of the more precisely known data on $r$-process nucleosynthesis calculations is investigated in light of these new mass measurements, showing a remarkable reduction of reaction-rate uncertainties.

## I. INTRODUCTION

The impact of nuclear structure effects on the $r$-process nucleosynthesis has been a topic of extensive research in nuclear astrophysics [1]. Subshell closures can significantly alter the path of the $r$-process and so the production of heavy elements. Specifically, shell and subshell closures lead to slower neutron capture rates causing a bottleneck in the path of the $r$-process. This results in abundance peaks and impacts the local abundance pattern in a specific mass region. As one of the most fundamental properties of atomic nuclei, mass plays an important role in the investigation of nuclear structure. Mass measurements provide access to two-neutron separation energies, $S_{2n}$, the evolution of which along the isotopic chains is shown to be a good index to study nuclear deformation and shell closures [2,3]. On the other hand, the (single) neutron separation energy, $S_n$, is one of the critical parameters for calculating neutron capture rates in the $r$-process.

The neutron-rich $A \approx 90$–100 region is of particular interest for nuclear astrophysics studies. In the nuclear structure point of view, this region is characterized by a rapid shape transition at $N = 60$ [4–7] and the subshell closure at $N = 56$ [8]. In the Zr ($Z = 40$) and Sr ($Z = 38$) isotopes in this region, dramatic shape changes from almost spherical to strongly deformed ground states were observed when the neutron number goes from $N = 58$ to $N = 60$ [9–12], which were interpreted as intruding deformed coexisting shapes [4,13,14].

*xianwd18@connect.hku.hk
†Present address: Department of Physics University of York, Heslington, York; sidong.chen@york.ac.uk

This rapid shape change was not observed in Kr ($Z = 36$) isotopes [15]. Instead, a picture of smooth onset of deformation was established based on mass measurements [16] and $\gamma$-ray spectroscopy [17]. A more recent $\gamma$-ray spectroscopic study of $^{98,100}$Kr isotopes found a significant increase of deformation beyond $N = 60$, shifted in neutron number compared to the sharp transition observed in Sr and Zr isotopes [18]. For the Se ($Z = 34$) isotopes, a smooth onset of deformation similar to Kr was suggested by the $\gamma$-ray spectroscopic measurements [19], but no mass data was available in this region. Accurate mass values were determined only up to $^{89}$Se ($N = 55$). Further mass measurements following the Se isotopic chain to more exotic nuclei are needed to provide complementary evidence for the deformation onset in Se isotopes.

An $N = 56$ subshell closure is found to occur around $Z = 40$, and is interpreted as the complete filling of the $\nu 2d_{5/2}$ orbital as shown in Fig. 3 of Ref. [20]. Mass [21] and $\gamma$-ray measurements [22,23] suggest that this shell gap vanishes in Kr isotopes. For Se isotopes, a $\gamma$-ray measurement in 2006 reported an anomalously high $E(2_1^+)$ of $^{88}$Se, and suggested a possible subshell effect at $N = 56$ for $^{90}$Se [24]. However, this $\gamma$ ray was not observed in later experiments for $^{88}$Se [19,25]. Both $\beta$-decay half-lives [26] and $\gamma$-ray signatures around $^{90}$Se [19,27] do not suggest an $N = 56$ subshell closure in the Se and lighter isotopes. From the mass measurement point of view, the $S_{2n}$ evolution of Se isotopes at $N = 56$ and beyond will provide direct experimental evidence for the existence or nonexistence of an $N = 56$ shell gap.

In astrophysics, although the creation of light $r$-process elements used to be attributed to neutrino-driven winds [28] in the aftermath of supernovae, nucleosynthesis in such scenarios is yet to be observed. Whereas, the observation of GW170817 followed by the kilonova event was the first direct evidence of the operation of the $r$-process in the aftermath of a neutron star merger (NSM) [29]. In addition, the identification of strontium ($Z = 38$) in the kilonova spectrum established NSM as a site of the $r$-process, hinting at the production of light elements [30].

Here, we present the first high-precision experimental results for the masses of $^{86}$Ge, $^{88,89}$As, and $^{90,91}$Se. The shell structure of these isotopes is discussed based on the evolution of the $S_{2n}$, and $r$-process nucleosynthesis calculations are performed to study the impact of the new mass data, in particular the impact on reaction rates and the abundances of strontium isotopes.

## II. EXPERIMENT

The measurements were performed at the RIBF facility [31] of the RIKEN Nishina Center (Japan). Radioactive isotopes were produced by in-flight fission of a $^{238}$U primary beam at an energy of 345 MeV/u, impinging on a $^9$Be production target. The isotopes of interest were selected and identified in the BigRIPS separator [32] for the preparation of the secondary beams. The present experiment was performed in parallel to in-beam $\gamma$-ray spectroscopy experiments, where the secondary beams impinged on a secondary target. Both reaction products and the unreacted beams were transported
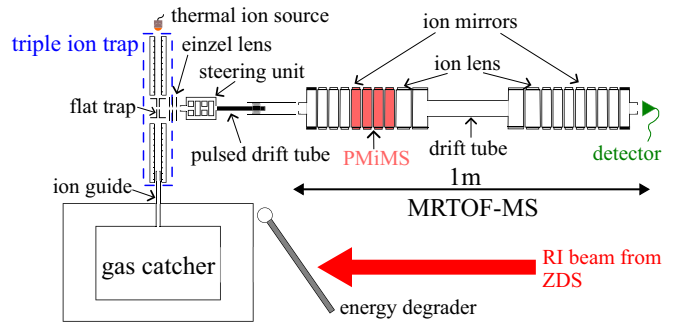


FIG. 1. Schematic of MRTOF-MS system at ZeroDegree spectrometer.

through the ZeroDegree (ZD) spectrometer [33] to the final position where the mass measurements were performed.

The ZeroDegree multi-reflection time-of-flight (ZD MRTOF) system [34] was set up after the last focal plane of the ZeroDegree spectrometer. As shown in Fig. 1, the ZD MRTOF system consisted of a cryogenic radiofrequency ion-guide helium gas catcher [35,36] and a recently assembled multi-reflection time-of-flight mass spectrograph (MRTOF-MS) [37]. Isotopes transported through ZeroDegree were first stopped in the gas catcher, then extracted to the MRTOF-MS for high-precision mass analysis. The isotopes exiting the ZeroDegree spectrometer have a typical energy of >100 MeV/u. An energy degrader system was developed to reduce the beam energy to match the stopping power of the helium gas [38]. Using the particle identification of ZeroDegree, the degrader thickness was adjusted during the experiment to optimize the stopping efficiency for individual isotopes [39].

The gas catcher was 500 mm long, pressurized to 200 mbar room temperature equivalent (helium gas density of $\approx 33 \, \mu g/cm^3$) and cooled down to a temperature of $\approx 180$ K. The extracted ions from the gas catcher were seen to be mostly singly charged [40]. The gas catcher and the MRTOF-MS were connected by an ion guide and a well-established triple ion trap suite reported in [41–43], which can accept ions independently from two directions: the gas catcher and a thermal ion source. In usual operation, the thermal ion source provided reference ions for system tuning, online calibration, and drift correction in offline analysis. The time-of-flight spectra of analyte ions and thermal ions were obtained in a concomitant referencing mode [43], i.e., analyte and reference measurements were performed sequentially in every 50 ms cycle (25 ms for each). Therefore, a software correction based on the TOF drift of thermal ions can be applied to the analyte ions [43]. For the $A \approx 90$ isotopes studied in this work, $^{85}$Rb$^+$ and $^{87}$Rb$^+$ from the thermal ion source were used to perform drift correction. However, isobaric ion species in the same subcycle of the analyte ions served as references for the mass determination of the radioactive ions.

The ions prepared in the flat trap were ejected perpendicularly to the MRTOF-MS. Before entering the MRTOF-MS, a pulsed drift tube was employed to adapt the ions to an average kinetic energy of 2.5 keV/q towards the MRTOF drift tube, which was at ground potential in this experiment. The
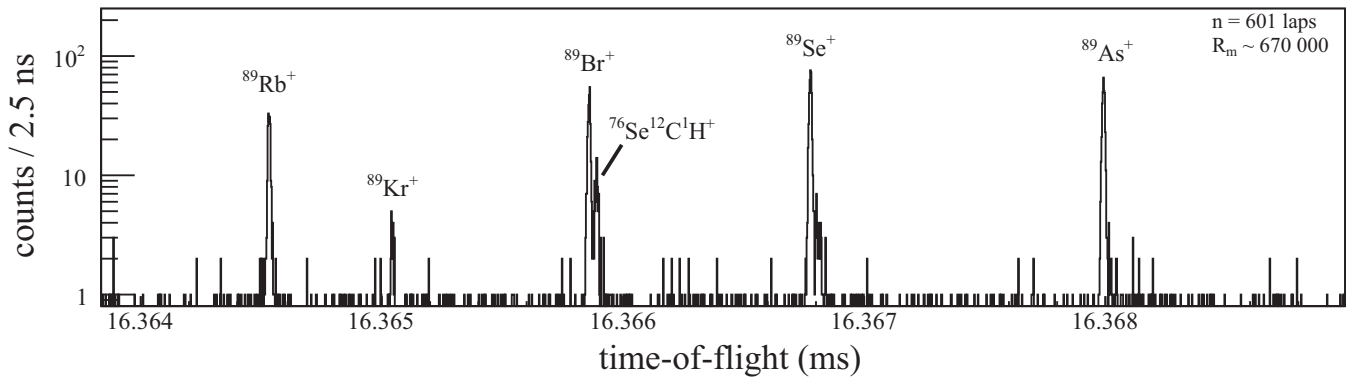
FIG. 2. Time-of-flight spectrum for $A = 89$ isobars after 601 laps in the MRTOF.

ions of interest were then reflected back and forth between the two concentric electrostatic mirrors of the MRTOF-MS for $n \approx 600$ laps before impacting on a fast TOF detector (MagneTOF, ETP Ion Detect Pty Ltd) [44]. The time-of-flight was measured as the duration from the flat trap ion ejection to the ion impact on the TOF detector, and recorded by a time-to-digital converter (TDC) model MCS6A with a digital resolution of 100 ps.

It was observed during the experiment that the ions from online beams were extracted from the gas catcher accompanied with a considerable amount of contaminant molecular ions, due to the ionization of the impurities in the gas catcher. Contaminant ions with similar mass-to-charge ratio to that of the ions of interest, were ejected from the MRTOF-MS and analyzed together with the ions of interest, which provided isobaric (well-known) mass references. Although the MRTOF-MS has a wide mass bandwidth to measure ions of different mass numbers simultaneously, a challenge for ion identification arose due to an exceeding amount of molecules of different mass numbers. To overcome this, a pulsed-mirror in-MRTOF selection (PMiMS) method was introduced to keep only isobaric ions in MRTOF-MS for the measurement of analyte ions [34,45].

### III. DATA ANALYSIS

An example of the time-of-flight spectra obtained in this experiment is shown in Fig. 2. The $^{89}$As and $^{89}$Se isotopes were provided by the ZeroDegree spectrometer and stopped in the gas catcher. Due to the short half-life of these isotopes, $\beta$ decay could occur before being analyzed by the MRTOF-MS, which produces other $A = 89$ isotopes towards the valley of stability. The PMiMS scheme was applied to keep only $A = 89$ ions. The spectrum was obtained at 601 laps, corresponding to times-of-flight of $\approx 16$ ms and a flight path of $\approx 1$ km. A mass resolving power $R_m = R_t/2 = t/2\Delta t$ of $\approx 670\,000$ was achieved in this experiment after performing drift correction. Peaks corresponding to $^{89}$As$^+$, $^{89}$Se$^+$ and their $\beta$-decay products are clearly visible in the spectrum.

Due to higher-order ion optical aberrations in the mirrors and low-angle scattering from the residual gas during flight, the peak in the spectrum has a slightly asymmetric shape. In order to extract the TOF by peak fitting with a decreased influence of the peak shape, the shape of the fitting function was

obtained by application of a sampling/smoothing algorithm to the ion peak in the reference spectrum (or any adequate high-intensity analyte ion peak of identical shape). The samples were obtained using averaging interpolation between the data points, while the fitting uncertainty for the numerical distribution was determined using a Monte Carlo approach as introduced in [46]. The peak position, peak width, and amplitude of the sample function were set as free parameters when fitting the most intense peak in the analyte ion spectrum. The peak width was then fixed when fitting other peaks in the same spectrum. Figure 3 shows the fitting for the $^{89}$As$^+$ peak from Fig. 2. The fitting function takes its shape from the $^{87}$Rb$^+$
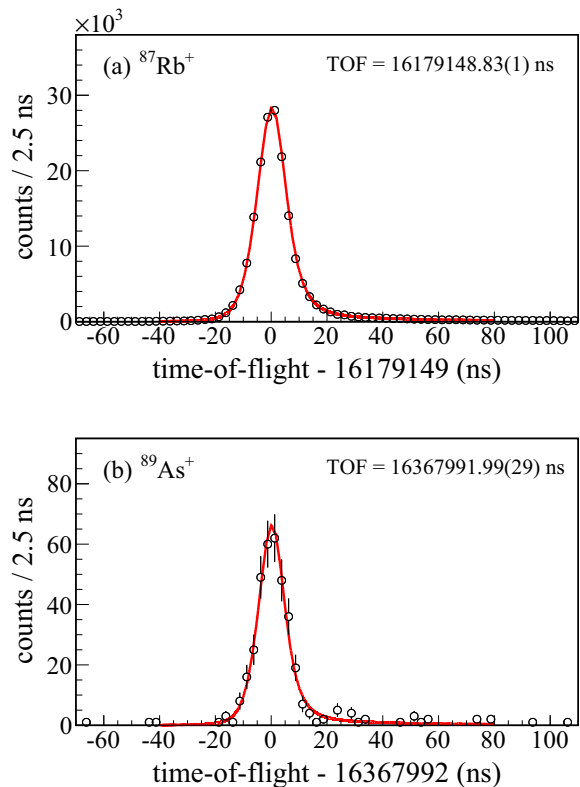


FIG. 3. Time-of-flight spectra for (a) $^{87}$Rb$^+$ and (b) $^{89}$As$^+$ after 601 laps in MRTOF. The fitting function takes its shape from the $^{87}$Rb$^+$ thermal ion peak.

(thermal ion source) spectrum in Fig. 3(a) and is fitted to the $^{89}$As$^+$ peak in Fig. 3(b).

For the MRTOF-MS, the time-of-flight $t$ of a singly charged ion is related to its mass $m$ by

$$t = a\sqrt{m} + t_0, \qquad (1)$$

where $a$ is a characteristic device constant and $t_0$ is the time difference between the TDC start signal and the actual ejection of ions towards the MRTOF-MS. For equally charged ions, the relation between masses and times-of-flight of two ions can be written as

$$m_1 = m_2\left(\frac{t_1 - t_0}{t_2 - t_0}\right)^2 = m_2\rho^2, \qquad (2)$$

where $\rho = (t_1 - t_0)/(t_2 - t_0)$ is the ratio of the effective times-of-flight. Using a well-known reference ion, the analyte ion mass is determined from the measured time-of-flight. An expansion of this equation to the first-order of $t_0$ yields

$$m_1 = m_2\left(\frac{t_1}{t_2}\right)^2 + 2m_2\frac{t_1(t_1 - t_2)}{t_2^3}t_0. \qquad (3)$$

As discussed in Ref. [42], the use of an isobaric reference ion, giving $(t_1 - t_2)/t_2$ in magnitude of $10^{-4}$ in this study and $t_0/t_2 \approx 10^{-5}$, results in a negligible mass uncertainty related to the uncertainty in $t_0$. Therefore, isobaric ion references were used for high-precision mass determinations in this study, and $t_0$ was fixed to a previously measured value $t_0 = 130$ ns, while the uncertainty of $t_0$ was omitted.

In the case of two well-known reference ions available, the relation between masses and times-of-flight of three ions can be written as

$$
\begin{aligned}
\sqrt{m_1} &= \left[\frac{2t_1 - t_2 - t_3}{2(t_2 - t_3)}\right](\sqrt{m_2} - \sqrt{m_3}) + \frac{\sqrt{m_2} + \sqrt{m_3}}{2} \\
&= C(\sqrt{m_2} - \sqrt{m_3}) + \frac{\sqrt{m_2} + \sqrt{m_3}}{2}, \qquad (4)
\end{aligned}
$$

where $C = (2t_1 - t_2 - t_3)/[2(t_2 - t_3)]$ comprises all measured times-of-flight [47]. In this method, the analyte ion mass is related to the masses of two well-known reference ions by times-of-flight without using $t_0$.

These two methods gave consistent results for the mass determinations for the ions measured in this work. To determine the masses in this study, we mainly applied the single reference method with isobaric references, while the double references method was used for $A = 83$ and $A = 84$ measurements, in which two well-known reference ions were available.

## IV. RESULTS

The derived mass excesses of radioactive isotopes measured in this work are listed in Table I. Birge ratios [48,49] are calculated when at least four independent measurements are available to evaluate the consistency of measurements for the same species.

The accuracy of the ZD MRTOF system was studied by evaluating the deviations of mass measurements of well-known stable atomic and molecular ions from AME2020

values. Various stable ions observed in most of the spectra with mass numbers 82–91 in this work provide abundant data to serve as isobaric references for the mass evaluation of radioactive species on one hand, or as benchmarks for a systematic accuracy study on the other. The mass measurements of 20 different ion species with uncertainties less than 0.5 keV in AME2020 are listed in Table II (see also Fig. 11 in [34]). As isobaric reference(s) is(are) utilized in the calculation, the mass-related systematic effect is negligible. The mass uncertainties of analytes in this analysis hence depend only on the statistical uncertainties of the TOF obtained for analyte and reference ions. As shown in Table II, most of the measurements of stable atomic or molecular ions agree well with AME2020 within one $\sigma$. The weighted mean deviation $\overline{\Delta m}$ of 1.2(0.8) keV reveals a high systematic accuracy of the mass values. The weighted standard deviation for previously known masses $\overline{\Delta m}$ in Table I is 3 keV, which is dominated by statistical fluctuations. Therefore an explicit treatment of systematic uncertainties is not meaningful for the present work.

## V. DISCUSSION

Figure 4 shows the evolution of two-neutron separation energies $S_{2n}$ as a function of the neutron number for Ge, As, and Se isotopes. $S_{2n}$ is extracted from mass values through the relation, $S_{2n}(Z, N) = M(Z, N-2)c^2 - M(Z, N)c^2 + 2M_nc^2$. The red-solid circles denote measurements in this work, while black triangles show the values from AME2020. Calculations by various models are plotted with colored dashed lines.

Figure 4(a) shows $S_{2n}$ values of the Ge isotopes. At $N = 54$, the $S_{2n}$ value was significantly improved through the reduction of uncertainty from 440 keV to 1.7 keV. A smooth monotonic decrease is observed from $N = 52$ to $N = 54$ of the Ge isotopes. Figure 4(b) shows $S_{2n}$ values of the As isotopes. The mass values of $^{88}$As and $^{89}$As have been experimentally determined for the first time with a high precision of 3.1 and 4.8 keV, respectively. Also for this case, a smooth decrease of the $S_{2n}$ values is observed from $N = 52$ to $N = 56$, suggesting no change in trend based on the newly obtained $S_{2n}$ values. Figure 4(c) shows the $S_{2n}$ values of the Se isotopes. At $N = 56$ and 57, the $S_{2n}$ values have been significantly improved with uncertainties down from 330 and 430 keV to 4.3 and 2.6 keV, respectively. Although the previous $S_{2n}$ value at $N = 57$ based on AME2020 exhibited a hint of flattening, a trend of consistent, smooth decrease is observed upon the improved $S_{2n}$ values at $N = 56$ and 57, suggesting there is no significant subshell effect at $N = 56$ of Se isotopes.

In Fig. 4, theoretical predictions of the masses for Ge, As, and Se isotopes are plotted using five popular mass models. The Duflo-Zuker [51] and HFB24 [52] models are classified as microscopic mass formulas which deduce the ground-state nuclear mass through Hartree-Fock calculations with a modeled nucleon-nucleon interaction. Contrarily, KTUY05 [53], WS4 + RBF [54], and FRDM12 [55] are classified as macroscopic-microscopic (macro-micro) models. These mass formulas usually treat the nucleus as a liquid drop in the macroscopic part. The microscopic part serves as the correction to the general trends of the mass surface by accounting for residual contributions such as shell and deformation effects.

TABLE I. Measured radioactive isotopes, the reference ion(s), square of effective time-of-flight ratios $\rho^2$, or the factor $C$ for double references, Birge-ratio $BR$ of the data sets, measured mass excess $ME_{MRTOF}$, mass excess from literature AME2020 [50], and mass deviation calculated as $\Delta m = ME_{MRTOF} - ME_{AME2020}$. Extrapolated values of AME2020 are denoted by #. The rule of rounding of ME refers to AME2020. The uncertainty for numeric values refer to the last digits of the value.

| Species | Ref. ion | $\rho^2$ or $C$ | $BR$ | $ME_{MRTOF}$ (keV/$c^2$) | $ME_{AME2020}$ (keV/$c^2$) | $\Delta m$ (keV/$c^2$) |
|---|---|---|---|---|---|---|
| $^{82}$Ge | $^{82}$Kr | 1.0001989197(132) | N/A | −65413.7(16) | −65415.1(22) | 1.4(28) |
| $^{82}$As | $^{82}$Kr | 1.0001374081(399) | N/A | −70107.2(33) | −70105.4(37) | −1.8(50) |
| $^{82}$Se | $^{82}$Kr | 1.0000393475(415) | N/A | −77589.8(34) | −77593.90(47) | 4.1(34) |
| $^{83}$Ga | $^{83}$Kr, $^{1}$H $^{12}$C $^{35}$Cl$_2$ | −0.550417(227) | N/A | −49260.8(71) | −49257.1(26) | −3.7(75) |
| $^{83}$Ge | $^{83}$Kr, $^{1}$H $^{12}$C $^{35}$Cl$_2$ | −0.149975(307) | N/A | −60975.6(92) | −60976.4(24) | 0.8(95) |
| $^{83}$As | $^{83}$Kr, $^{1}$H $^{12}$C $^{35}$Cl$_2$ | 0.147235(382) | N/A | −69670(11) | −69669.3(28) | −0.4(116) |
| $^{84}$Ga | $^{84}$Kr, $^{12}$C $^{35}$Cl $^{37}$Cl | −1.269866(263) | 0.62 | −44088.5(75) | −44094(30) | 6(31) |
| $^{84}$Ge | $^{84}$Kr, $^{12}$C $^{35}$Cl $^{37}$Cl | −0.6210181(541) | 0.61 | −58148.0(30) | −58148.4(32) | 0.5(44) |
| $^{84}$As | $^{84}$Kr, $^{12}$C $^{35}$Cl $^{37}$Cl | −0.2652515(948) | 1.10 | −65853.5(41) | −65853.6(32) | 0.1(52) |
| $^{84}$Se | $^{84}$Kr, $^{12}$C $^{35}$Cl $^{37}$Cl | 0.2005865(871) | 1.53 | −75952.5(47) | −75947.7(20) | −4.8(51) |
| $^{85}$Ge | $^{84}$Kr $^{1}$H | 1.0002785543(642) | N/A | −53116.2(55) | −53123.4(37) | 7.2(66) |
| $^{85}$As | $^{84}$Kr $^{1}$H | 1.0001511118(129) | 2.10 | −63196.4(28) | −63189.2(31) | −7.3(41) |
| $^{85}$Se | $^{84}$Kr $^{1}$H | 1.0000345699(235) | 0.96 | −72415.9(20) | −72413.7(26) | −2.2(33) |
| $^{85}$Br | $^{84}$Kr $^{1}$H | 0.999956405(146) | 0.80 | −78599(12) | −78575.5(31) | −23(12) |
| $^{86}$Ge | $^{86}$Kr | 1.0004207308(139) | 1.04 | −49596.7(17) | −49400(440) | −200(440) |
| $^{86}$As | $^{86}$Kr | 1.0003036665(198) | 0.72 | −58964.6(20) | −58962.2(35) | −2.5(40) |
| $^{86}$Se | $^{86}$Kr | 1.00015948638(965) | 0.81 | −70503.5(12) | −70503.2(25) | −0.3(28) |
| $^{86}$Br | $^{86}$Kr | 1.0000953104(188) | 0.75 | −75638.4(17) | −75632.3(31) | −6.1(35) |
| $^{87}$As | $^{86}$Kr $^{1}$H | 1.0002514569(324) | N/A | −55617.8(29) | −55617.9(30) | 0.1(42) |
| $^{87}$Se | $^{86}$Kr $^{1}$H | 1.0001179997(355) | N/A | −66425.3(32) | −66426.1(22) | 0.9(39) |
| $^{88}$As | $^{88}$Br | 1.0002446318(273) | 0.99 | −50677.8(31) | −50450#(200#) | −230#(200#) |
| $^{88}$Se | $^{88}$Br | 1.0000834436(107) | 0.48 | −63882.5(21) | −63884.2(34) | 1.7(40) |
| $^{89}$As | $^{89}$Rb | 1.0004229057(396) | N/A | −46686.5(48) | −46530#(300#) | −160#(300#) |
| $^{89}$Se | $^{89}$Rb | 1.0002743663(387) | N/A | −58989.4(48) | −58992.4(37) | 3.0(61) |
| $^{89}$Br | $^{89}$Rb | 1.0001622379(402) | N/A | −68275.0(48) | −68274.3(33) | −0.7(58) |
| $^{89}$Kr | $^{89}$Rb | 1.000062495(122) | N/A | −76537(12) | −76535.8(21) | −1(12) |
| $^{90}$Se | $^{90}$Kr | 1.0002277746(470) | 0.88 | −55881.3(43) | −55800(330) | −80(330) |
| $^{90}$Br | $^{90}$Kr | 1.0001308598(477) | 0.87 | −63998.8(43) | −64000.3(34) | 1.5(55) |
| $^{90}$Rb | $^{90}$Kr | 0.9999475458(524) | 1.14 | −79352.3(53) | −79365.6(65) | 13.2(83) |
| $^{91}$Se | $^{79}$Br $^{12}$C | 1.0003046507(257) | N/A | −50267.4(26) | −50580(430) | 310(430) |
| $^{91}$Br | $^{79}$Br $^{12}$C | 1.0001766579(229) | N/A | −61106.8(25) | −61107.3(35) | 0.5(44) |
| $^{91}$Kr | $^{79}$Br $^{12}$C | 1.0000601829(644) | N/A | −70971.1(57) | −70974.0(22) | 2.9(61) |
| $^{91}$Rb | $^{79}$Br $^{12}$C | 0.9999800114(225) | N/A | −77760.6(24) | −77745.1(78) | −15.5(82) |
| $^{92}$Br | $^{78}$Se $^{12}$C $^{1}$H$_2$ | 1.0000724875(722) | N/A | −56240.5(64) | −56232.8(67) | −7.7(93) |
| $^{92}$Kr | $^{78}$Se $^{12}$C $^{1}$H$_2$ | 0.9999261505(977) | N/A | −68772.0(85) | −68769.3(27) | −2.7(90) |

Figure 5 shows the difference of mass excesses of various mass models to measurements made in this work. Mass excesses calculated using Duflo-Zuker model in the region of interest, values are always underestimated. However, the deviations are reduced towards higher $Z$ and $N$ numbers. Except for the chain of As ($Z = 33$), a moderate odd-even staggering is seen. The WS4 + RBF model has the smallest root-mean-square (rms) deviation (170 keV) from experimental values among the macro-micro mass models [54]. Comparison with measurements made in this work, it maintains the best agreements on average with an odd-even staggering (<500 keV) along $N = 51 - 55$. KTUY05 and HFB24 show similar reasonably good agreements with our measurements. However, KTUY05 agrees best with the improved or newly determined mass values of $^{86}$Ge and $^{89}$As, respectively. Although the rms deviation from AME2003 is limited to 560 keV [55], the

FRDM12 shows a significantly large deviation ($>10^3$ keV) at $N = 53$ for both isotopic chains under investigation. The reason for these deviations could be that the model expects $N = 54$ a watershed of different shell closure deterioration, which can also be observed in plots of $S_{2n}$ evolution in Fig. 4.

## VI. IMPACT TO THE *r*-PROCESS

### A. The Hauser-Feshbach statistical model

The Hauser-Feshbach statistical model [56,57] is a widely used theoretical framework for understanding nuclear reactions involving the compound nucleus. According to the concept, a nuclear reaction's compound nucleus can decay through a statistical emission of particles or $\gamma$ rays, leading to the creation of reaction byproducts. The model is founded on

TABLE II. Measurements of stable atomic and molecular ions and the corresponding mass deviations($\Delta m = \text{ME}_{\text{MRTOF}} - \text{ME}_{\text{AME2020}}$) from AME2020. The rule of rounding of ME refers to AME2020. The uncertainty for numeric values refer to the last digits of the value.

| Mass number | Species | Ref. ion | $\text{ME}_{\text{MRTOF}}$ (keV/$c^2$) | $\text{ME}_{\text{AME2020}}$ (keV/$c^2$) | $\Delta m$ (keV/$c^2$) |
|---|---|---|---|---|---|
| 82 | $^{82}$Se | $^{82}$Kr | −77589.8(34) | −77593.90(47) | 4.1(34) |
| 83 | $^{82}$Kr $^1$H | $^{83}$Kr, $^1$H $^{12}$C $^{35}$Cl$_2$ | −73307.7(49) | −73302.8240(55) | −4.9(49) |
| 84 | $^{83}$Kr $^1$H | $^{84}$Kr, $^{12}$C $^{35}$Cl $^{37}$Cl | −72701.1(23) | −72701.6728(84) | 0.6(23) |
| 84 | $^{13}$C $^1$H $^{35}$Cl$_2$ | $^{84}$Kr, $^{12}$C $^{35}$Cl $^{37}$Cl | −47615.4(45) | −47613.083(71) | −2.3(45) |
| 84 | $^{12}$C $^1$H$_2$ $^{16}$O $^{19}$F $^{35}$Cl | $^{84}$Kr, $^{12}$C $^{35}$Cl $^{37}$Cl | −20655.3(57) | −20660.037(35) | 4.7(57) |
| 84 | $^{12}$C$_4$ $^1$H$_4$ $^{32}$S | $^{84}$Kr, $^{12}$C $^{35}$Cl $^{37}$Cl | 3138.4(35) | 3140.3471(13) | −2.0(35) |
| 84 | $^{12}$C $^{35}$Cl $^{37}$Cl | $^{84}$Kr, $^{12}$C $^{35}$Cl $^{37}$Cl | −60774.4(27) | −60775.084(62) | 0.7(27) |
| 85 | $^{12}$C $^1$H $^{35}$Cl $^{37}$Cl | $^{84}$Kr $^1$H | −53485.9(28) | −53486.113(62) | 0.2(28) |
| 86 | $^{12}$C $^{37}$Cl$_2$ | $^{86}$Kr | −63522.3(22) | −63523.10(10) | 0.8(22) |
| 86 | $^{13}$C $^1$H $^{35}$Cl $^{37}$Cl | $^{86}$Kr | −50359.9(34) | −50361.104(62) | 1.2(34) |
| 86 | $^{12}$C $^1$H$_4$ $^{35}$Cl$_2$ | $^{86}$Kr | −28866.1(26) | −28871.179(71) | 5.1(26) |
| 87 | $^{12}$C $^1$H $^{37}$Cl$_2$ | $^{86}$Kr $^1$H | −56231.7(25) | −56234.13(10) | 2.4(25) |
| 88 | $^{12}$C$_4$ $^1$H$_2$ $^{19}$F$_2$ | $^{88}$Br | 11613(13) | 11603.0519(16) | 10(13) |
| 88 | $^{12}$C $^1$H$_4$ $^{35}$Cl $^{37}$Cl | $^{88}$Br | −31608.5(60) | −31619.200(60) | 10.7(60) |
| 88 | $^{12}$C$_2$ $^{16}$O$_4$ | $^{88}$Br | −18954.4(88) | −18948.0087(12) | −6.4(88) |
| 89 | $^{76}$Se $^{12}$C $^1$H | $^{89}$Rb | −67964.7(54) | −67962.989(16) | −1.7(54) |
| 90 | $^{76}$Se $^{12}$C $^1$H$_2$ | $^{90}$Kr | −60676.3(61) | −60674.018(16) | −2.3(61) |
| 90 | $^{77}$Se $^{12}$C $^1$H | $^{90}$Kr | −67297.1(94) | −67310.526(62) | 13.4(94) |
| 91 | $^{78}$Se $^{12}$C $^1$H | $^{79}$Br $^{12}$C | −69733.3(31) | −69736.98(18) | 3.7(31) |
| 91 | $^{77}$Se $^{12}$C $^1$H$_2$ | $^{79}$Br $^{12}$C | −60024.7(40) | −60021.555(62) | −3.2(40) |

the idea of the compound nucleus and necessitates an understanding of reaction cross sections and nuclear level densities.

Nuclear masses play a critical role in the Hauser-Feshbach statistical model as they determine the available energy for the reaction, and hence the probability of various decay channels. In particular, the masses of the target and projectile nuclei, as well as the compound nucleus, must be known with high accuracy to predict the reaction outcomes.

Using the HF statistical code TALYS [58], we calculated neutron capture reaction rates to determine the effect of the new mass measurements. To take into consideration the effects of nuclear structure and interactions between particles and $\gamma$ rays, we used the Konig-Delaroche optical potential [59], the back-shifted Fermi gas level density [60], and the Kopecky-Uhl generalized Lorentzian $E1$ $\gamma$-ray strength function [61]. Experimental data from AME2020 and NUBASE20 [62] was employed, when available, or we employ FRDM12 [55] for unknown nuclear mass values.

To assess the impact of nuclear mass uncertainties on the *r*-process, we calculated reaction rates using the central, upper limit, and lower limit of the experimental mass values, and compared them to the AME2020 mass values and uncertainties. We also compared our results to the FRDM 2020 mass values. The calculated reaction rates are presented in Fig. 6 as color-coded boxes, defined as an index $I$ given by $< \sigma v >_{\text{exp}} / < \sigma v >_{\text{AME}}$, where $< \sigma v >_{\text{exp}}$ and $< \sigma v >_{\text{AME}}$ indicate the reaction rate based on our experimental results and on AME2020, respectively.

Our findings demonstrate a significant impact of the mass measurements on the calculated reaction rates. In some cases, the changes have been more than a factor of two compared to the corresponding reaction rate calculations based on the

AME2020. The most substantial changes in the calculated neutron capture reaction rates were observed for $^{86}$Ge, $^{88,89}$As, and $^{90,91}$Se, where the mass measurements differed from the AME2020 mass values by hundreds of keV, as expected.

Similarly, to visualize the reduction in uncertainties of the reaction rate calculations, we calculate an index $I_{\text{error}}$ as

$$I_{\text{error}} = \frac{\text{Max}(< \sigma v >_{\text{exp}}) - \text{Min}(< \sigma v >_{\text{exp}})}{\text{Max}(< \sigma v >_{\text{AME}}) - \text{Min}(< \sigma v >_{\text{AME}})}. \quad (5)$$

Figure 7 shows an $N - Z$ plane plot with a color-coded representation of the index $I_{\text{error}}$, where the colors indicate different magnitudes of reduction in uncertainty. Specifically, the measurements of $^{86}$Ge and their impact on the $^{85}$Ge$(n, \gamma)$$^{86}$Ge and $^{86}$Ge$(\gamma, n)$$^{85}$Ge reactions demonstrate a reduction in the ratio of uncertainties by an order of magnitude or more. Similarly, the results for $^{88}$As and $^{88}$Se are consistent with expectations, as previous measurements (or extrapolations in the case of As) had large mass error bars in AME2020, corresponding to hundreds of keV. With the latest measurements, these error bars have been significantly reduced to less than 10 keV, resulting in more precise data and confirming the significance of the results.

### B. *r*-process nucleosynthesis calculations

We used the calculated reaction rates described in Sec. VI A to assess the impact of the new mass measurements on the *r*-process nucleosynthesis. A parametrized thermodynamic evolution assuming a free homologous expansion according to Ref. [63] was used for astrophysical conditions with an electron fraction $0.30 \leqslant Y_e \leqslant 0.42$ and entropy $S = 10 \, k_b$/baryon.
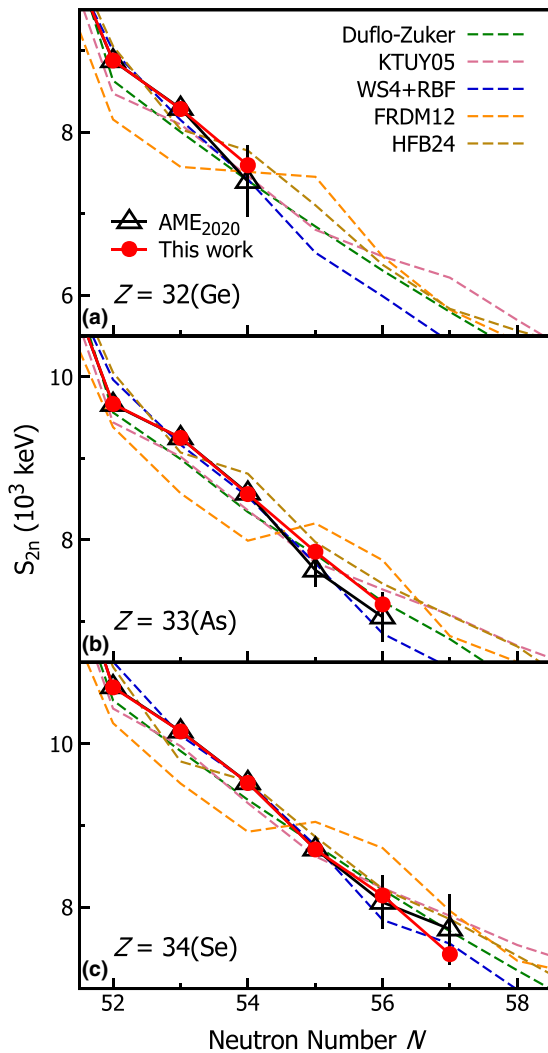
FIG. 4. Comparison of experimental two-neutron separation energies, $S_{2n}$ with calculated results from five popular mass models. Plots (a), (b), and (c) show $S_{2n}$ systematics of the isotopic chains of Ge, As, and Se, respectively. Dashed curves are calculations from corresponding models, while red-solid and black circles are experimental values from the ZD MRTOF system and AME2020, respectively.

Figure 8 shows the solar $r$-process abundances from Ref. [64], together with the result from the $r$-process calculations presented in this work. The abundances $Y$ are determined as $Y = X/A$, where $X$ is the mass fraction. The normalization is arbitrary to provide the best match to the observed abundances. We observe differences of up to 20% compared to AME2020 to the abundances for elements with mass number $A = 85$–95 due to the mass measurements, which propagate to higher mass numbers. Specifically, we observe no drastic changes to the structure of the abundance pattern but rather a shift that is enabled by the differences in the reaction rate in this moderately neutron-rich environment. While these changes are not drastic, the affected area is of particular interest. Specifically, predictions of the production of strontium ($A = 88$) are of importance, as this remains the only element
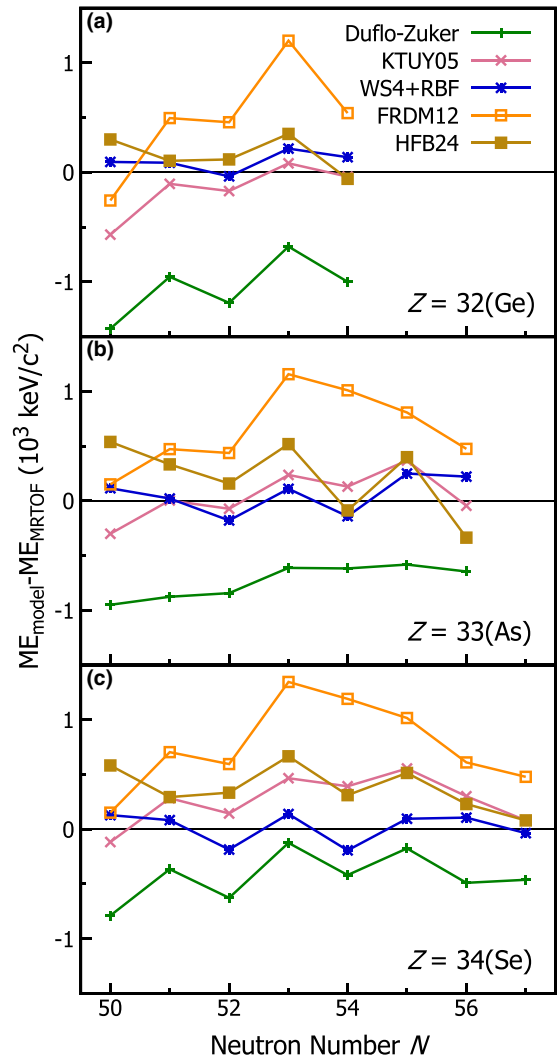


FIG. 5. Difference of mass excess values from calculations and measurements of Ge(a), As(b), and Se(c).
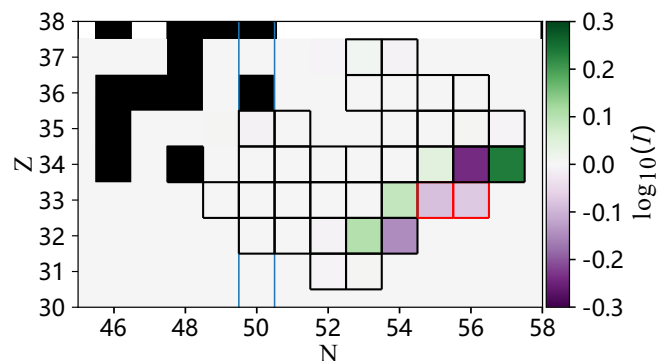


FIG. 6. $N - Z$ plane where with color code represents the logarithm of the ratio ($I$) of reaction rates calculated in the bases of the new experimental mass values over reaction rates calculated using AME2020. Black borders represent the measured masses. Red squares are masses measured for the first time in this study. Filled squares represent stable elements.
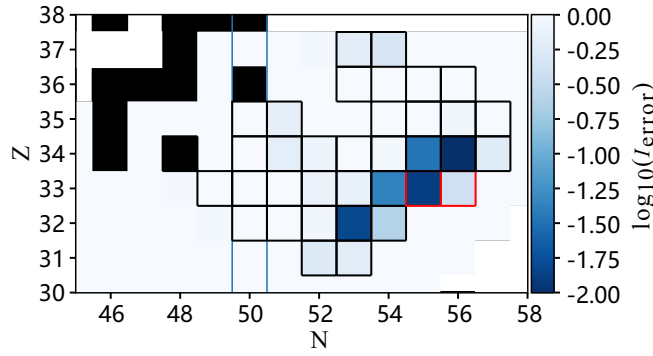
FIG. 7. Same as Fig. 6 but with the color code representing the logarithm of the ratio ($I_{error}$) of reaction rate uncertainties.

identified in the nucleosynthesis event following the detection of gravitational waves of the event GW170817 [29,30]. While the astrophysical conditions behind the NSM event are far from being constrained, the mass measurements add a piece to the puzzle of the *r*-process nucleosynthesis reducing the corresponding uncertainties and confining the production of elements of interest such as Sr. Figure 9 displays the abundances of Sr isotopes as a function of time for both newly measured masses and masses from AME2020, including their corresponding uncertainties. Our results show that significant
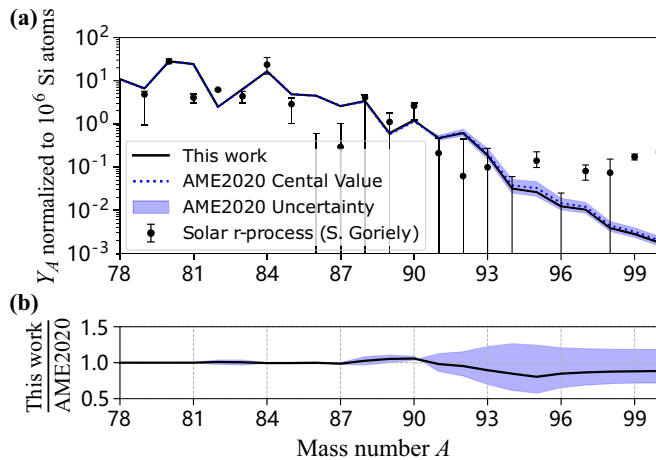


FIG. 8. A. The figure displays abundances vs. mass number $A$ for elements near the first *r*-process peak. The abundances based on newly measured masses are represented by a black line, while those from the AME2020 database are depicted with a dotted blue line. Both sets of abundances are accompanied by their respective error bars (shaded areas). The solar *r*-process abundances and associated uncertainties, taken from [65], are illustrated by the black error bars. We assume a uniform $Y_e$ distribution in the range $0.34 \leqslant Y_e \leqslant 0.38$. The blue-shaded area marks uncertainties stemming from experimental values in the AME2020 database. In contrast, the black area highlights the impact of experimental mass uncertainties from our study. Notably, the uncertainty band from our measurements is now indistinguishable. B. The plot illustrates the ratio of abundances from our work compared to those from the AME2020 database, revealing relative differences. The blue line signifies the main ratio, and the blue band encompasses uncertainties from AME2020.
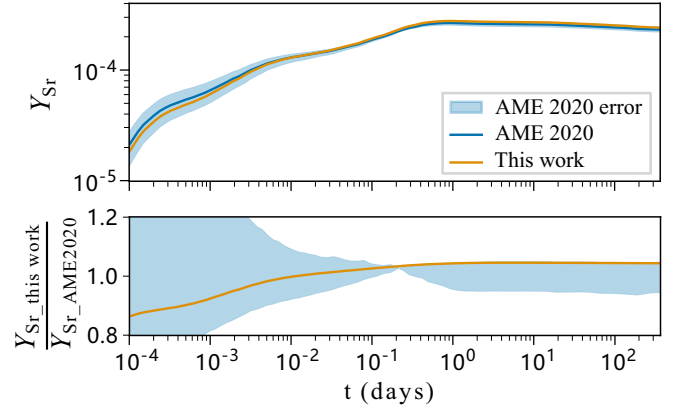


FIG. 9. Top panel: Abundances of Sr isotopes vs. time in days assuming the newly measured masses and masses of AME2020 within their error bar in a logarithmic scale. We consider the same uniform distribution of $Y_e$ such as $0.34 \leqslant Y_e \leqslant 0.38$, as in Fig. 8. Bottom panel: The ratio between the abundances obtained from this work to the abundances derived from the AME2020 database indicates relative differences.

changes of up to 20% compared to the central values in AME2020 are observed during nucleosynthesis. However, at later times, these differences become smaller, with variations typically within the 5% range.

## VII. CONCLUSION

The masses of $^{83,84}$Ga, $^{82-86}$Ge, $^{82-89}$As, $^{82,84-91}$Se, $^{85,86,89-92}$Br, $^{89,91,92}$Kr, and $^{91}$Rb have been determine accurately and with high precision in the first online commissioning measurement of the ZD MRTOF-MS. Among the 35 nuclides measured in this work, masses of $^{88,89}$As are evaluated for the first time, while the uncertainties of $^{86}$Ge and $^{90,91}$Se have been improved significantly from hundreds of keV to less than 10 keV. Comparison to mass models, with the inputs of new mass values, showed WS4 + RBF best reproduces the mass excesses of the isotopic chains in the discussion. Except for FRDM12, mass models used here manifest similar $S_{2n}$ curves agreeing reasonably with observations. Both predictions and experimental values of $S_{2n}$ indicate a smooth evolution of neutron shell in the region of interest. According to the trend of $S_{2n}$, no significant change on the slope has been observed, which indicates that a $N = 56$ subshell closure for Se does not exist. Although precise mass data of more neutron-rich nuclei are highly desired to draw a conclusion on the shell evolution of the Se isotopic chain, measurements in this work have proceeded one step further toward mass evaluation of more exotic isotopes. To assess the impact of the measured masses on the *r*-process, the Hauser-Feshbach statistical model was utilized to calculate nuclear reaction rates, incorporating the associated propagated uncertainties. These reaction rates were then employed in *r*-process nucleosynthesis calculations to investigate changes in element abundances. The study focused on a narrow range of $Y_e$ values, corresponding to trajectories consistent with the modeling of neutron star merger outflows [63,66]. The

[1] H. Grawe, K. Langanke, and G. Martínez-Pinedo, Nuclear structure and astrophysics, Rep. Prog. Phys. **70**, 1525 (2007).

[2] R. Fossion, C. De Coster, J. Garca-Ramos, T. Werner, and K. Heyde, Nuclear binding energies: Global collective structure and local shell-model correlations, Nucl. Phys. A **697**, 703 (2002).

[3] U. Hager, T. Eronen, J. Hakala, A. Jokinen, V. S. Kolhinen, S. Kopecky, I. Moore, A. Nieminen, M. Oinonen, S. Rinta-Antila, J. Szerypo, and J. Äystö, First precision mass measurements of refractory fission fragments, Phys. Rev. Lett. **96**, 042504 (2006).

[4] K. Heyde and J. L. Wood, Shape coexistence in atomic nuclei, Rev. Mod. Phys. **83**, 1467 (2011).

[5] K. Sieja, F. Nowacki, K. Langanke, and G. Martínez-Pinedo, Shell model description of zirconium isotopes, Phys. Rev. C **79**, 064310 (2009).

[6] P. Sarriguren, $\beta$-decay properties of neutron-rich Ge, Se, Kr, Sr, Ru, and Pd isotopes from deformed quasiparticle random-phase approximation, Phys. Rev. C **91**, 044304 (2015).

[7] T. R. Rodríguez, Structure of krypton isotopes calculated with symmetry-conserving configuration-mixing methods, Phys. Rev. C **90**, 034306 (2014).

[8] T. Werner, J. Dobaczewski, M. Guidry, W. Nazarewicz, and J. Sheikh, Microscopic aspects of nuclear deformation, Nucl. Phys. A **578**, 1 (1994).

[9] P. Federman and S. Pittel, Towards a unified microscopic description of nuclear deformation, Phys. Lett. B **69**, 385 (1977).

[10] G. Lhersonneau, B. Pfeiffer, K.-L. Kratz, H. Ohm, and K. Sistemich, Shape coexistence in the $N = 59$ isotone $^{97}$Sr, Z. Phys. A: At. Nucl. **330**, 347 (1988).

[11] M. A. C. Hotchkis, J. L. Durell, J. B. Fitzgerald, A. S. Mowbray, W. R. Phillips, I. Ahmad, M. P. Carpenter, R. V. F. Janssens, T. L. Khoo, E. F. Moore, L. R. Morss, Ph. Benet, and D. Ye, New neutron-rich nuclei $^{103,104}$Zr and the $A \sim 100$ region of deformation, Phys. Rev. Lett. **64**, 3123 (1990).

[12] W. Urban, J. A. Pinston, J. Genevey, T. Rzaca-Urban, A. Złomaniec, G. Simpson, J. L. Durell, W. R. Phillips, A. G. Smith, B. J. Varley, I. Ahmad, and N. Schulz, The $\nu 9/2$ [404] orbital and the deformation in the $A \sim 100$ region, Eur. Phys. J. A **22**, 241 (2004).

[13] T. Togashi, Y. Tsunoda, T. Otsuka, and N. Shimizu, Quantum phase transition in the shape of Zr isotopes, Phys. Rev. Lett. **117**, 172502 (2016).

[14] E. Clément *et al.*, Spectroscopic quadrupole moments in $^{96,98}$Sr: Evidence for shape coexistence in neutron-rich strontium isotopes at $N = 60$, Phys. Rev. Lett. **116**, 022701 (2016).

[15] J. Dudouet *et al.*, $^{96}_{36}$Kr$_{60}$ -Low-$Z$ boundary of the island of deformation at $N = 60$, Phys. Rev. Lett. **118**, 162501 (2017).

[16] S. Naimi *et al.*, Critical-point boundary for the nuclear quantum phase transition near $A = 100$ from mass measurements of $^{96,97}$Kr, Phys. Rev. Lett. **105**, 032502 (2010).

[17] M. Albers *et al.*, Evidence for a smooth onset of deformation in the neutron-rich Kr isotopes, Phys. Rev. Lett. **108**, 062701 (2012).

[18] F. Flavigny *et al.*, Shape evolution in neutron-rich krypton isotopes beyond $N = 60$: First spectroscopy of $^{98,100}$Kr, Phys. Rev. Lett. **118**, 242501 (2017).

[19] S. Chen *et al.*, Low-lying structure and shape evolution in neutron-rich se isotopes, Phys. Rev. C **95**, 041302 (2017).

[20] J. A. Winger *et al.*, New subshell closure at $N = 58$ emerging in neutron-rich nuclei beyond $^{78}$Ni, Phys. Rev. C **81**, 044303 (2010).

[21] P. Delahaye *et al.*, High-accuracy mass measurements of neutron-rich Kr isotopes, Phys. Rev. C **74**, 034331 (2006).

[22] K.-L. Kratz, H. Gabelmann, B. Pfeiffer, and P. Möller, Onset of deformation in neutron-rich krypton isotopes, Z. Phys. A: At. Nucl. **330**, 229 (1988).

[23] D. Mücher *et al.*, Shell structure and shape changes in neutron rich krypton isotopes, AIP Conf. Proc. **1090**, 587 (2009).

[24] E. F. Jones *et al.*, Identification of $^{88}$Se and new levels in $^{84,86}$Se, Phys. Rev. C **73**, 017301 (2006).

[25] I. N. Gratchev, G. S. Simpson, G. Thiamova, M. Ramdhane, K. Sieja, A. Blanc, M. Jentschel, U. Köster, P. Mutti, T. Soldner, G. de France, C. A. Ur, and W. Urban, Identification of excited states and collectivity in $^{88}$Se, Phys. Rev. C **95**, 051302(R) (2017).

[26] M. Quinn *et al.*, $\beta$ decay of nuclei around $^{90}$se: Search for signatures of a $N = 56$ subshell closure relevant to the *r* process, Phys. Rev. C **85**, 035807 (2012).

[27] M. Lettmann *et al.*, Triaxiality of neutron-rich $^{84,86,88}$Ge from low-energy nuclear spectra, Phys. Rev. C **96**, 011301(R) (2017).

[28] A. Arcones and F. Montes, Production of light-element primary process nuclei in neutrino-driven winds, Astrophys. J. **731**, 5 (2011).

[29] B. P. Abbott, R. Abbott, T. Abbott, F. Acernese, K. Ackley, C. Adams, T. Adams, P. Addesso, R. Adhikari, V. Adya *et al.*, GW170817: Observation of gravitational waves from a binary neutron star inspiral, Phys. Rev. Lett. **119**, 161101 (2017).

[30] D. Watson, C. J. Hansen, J. Selsing, A. Koch, D. B. Malesani, A. C. Andersen, J. P. Fynbo, A. Arcones, A. Bauswein, S. Covino *et al.*, Identification of strontium in the merger of two neutron stars, Nature (London) **574**, 497 (2019).

[31] Y. Yano, The RIKEN RI beam factory project: A status report, Nucl. Instrum. Methods Phys. Res. B **261**, 1009 (2007).

[32] T. Kubo, In-flight RI beam separator bigrips at RIKEN and elsewhere in Japan, Nucl. Instrum. Methods Phys. Res. B **204**, 97 (2003).

[33] T. Kubo *et al.*, Bigrips separator and ZeroDegree spectrometer at Riken Ri beam factory, Prog. Theor. Exp. Phys. **2012**, 03C003 (2012).

[34] M. Rosenbusch *et al.*, The new MRTOF mass spectrograph following the ZeroDegree spectrometer at Riken's RIBF facility, Nucl. Instrum. Methods Phys. Res. A **1047**, 167824 (2023).

[35] M. Wada *et al.*, Slow Ri-beams from projectile fragment separators, Nucl. Instrum. Methods Phys. Res. B **204**, 570 (2003).

[36] A. Takamine *et al.*, Offline test for RF carpet transportation in RF ion guide gas cell at the SLOWRI facility, RIKEN Accel. Prog. Rep. **52**, 139 (2019).

[37] M. Rosenbusch *et al.*, A new multi-reflection time-of-flight mass spectrograph for the SLOWRI facility, Nucl. Instrum. Methods Phys. Res. B **463**, 184 (2020).

[38] J. Liu *et al.*, Degrader system for ZD-MRTOF, RIKEN Accel. Prog. Rep. **53**, 133 (2020).

[39] S. Chen *et al.*, Degrader optimization for ZeroDegree gas cell, RIKEN Accel. Prog. Rep. **54**, 97 (2021).

[40] D. Hou *et al.*, Temperature and pressure dependence of ion extraction from RF gas cell, RIKEN Accel. Prog. Rep. **54**, 96 (2021).

[41] Y. Ito *et al.*, A novel ion cooling trap for multi-reflection time-of-flight mass spectrograph, Nucl. Instrum. Methods Phys. Res. B **317**, 544 (2013).

[42] P. Schury, M. Wada, Y. Ito, F. Arai, S. Naimi, T. Sonoda, H. Wollnik, V.A. Shchepunov, C. Smorra, and C. Yuan, A high-resolution multi-reflection time-of-flight mass spectrograph for precision mass measurements at RIKEN/SLOWRI, Nucl. Instrum. Methods Phys. Res. B **335**, 39 (2014).

[43] Y. Ito *et al.*, First direct mass measurements of nuclides around $Z = 100$ with a multireflection time-of-flight mass spectrograph, Phys. Rev. Lett. **120**, 152501 (2018).

[44] https://www.etp-ms.com/file-repository/8.

[45] S. Yan *et al.*, Removing non-isobaric ions from an MRTOF-MS by periodic electric pulses, RIKEN Accel. Prog. Rep. **54**, S28 (2021).

[46] A. V. Chudinov, M. Rosenbusch, V. I. Kozlovskiy, V. V. Raznikov, P. Schury, M. Wada, and H. Wollnik, Model independent peak fitting and uncertainty assignment for high-precision time-of-flight mass spectrometry, Analyst **145**, 3401 (2020).

[47] F. Wienholtz, D. Beck, K. Blaum, C. Borgmann, M. Breitenfeldt, R. B. Cakirli, S. George, F. Herfurth, J. Holt, M. Kowalska *et al.*, Masses of exotic calcium isotopes pin down nuclear forces, Nature (London) **498**, 346 (2013).

[48] R. T. Birge, The calculation of errors by the method of least squares, Phys. Rev. **40**, 207 (1932).

[49] O. Bodnar and C. Elster, On the adjustment of inconsistent data using the Birge ratio, Metrologia **51**, 516 (2014).

[50] M. Wang, W. Huang, F. Kondev, G. Audi, and S. Naimi, The AME 2020 atomic mass evaluation (II). Tables, graphs and references, Chin. Phys. C **45**, 030003 (2021).

[51] J. Duflo and A. P. Zuker, Microscopic mass formulas, Phys. Rev. C **52**, R23 (1995).

[52] S. Goriely, N. Chamel, and J. M. Pearson, Further explorations of Skyrme-Hartree-Fock-Bogoliubov mass formulas. XIII. The 2012 atomic mass evaluation and the symmetry coefficient, Phys. Rev. C **88**, 024308 (2013).

[53] H. Koura, T. Tachibana, M. Uno, and M. Yamada, Nuclidic mass formula on a spherical basis with an improved even-odd term, Prog. Theor. Phys. **113**, 305 (2005).

[54] N. Wang, M. Liu, X. Wu, and J. Meng, Surface diffuseness correction in global mass formula, Phys. Lett. B **734**, 215 (2014).

[55] P. Möeller, A. Sierk, T. Ichikawa, and H. Sagawa, Nuclear ground-state masses and deformations: FRDM(2012), At. Data Nucl. Data Tables **109–110**, 1 (2016).

[56] W. Hauser and H. Feshbach, The inelastic scattering of neutrons, Phys. Rev. **87**, 366 (1952).

[57] P. Moldauer, Why the Hauser-Feshbach formula works, Phys. Rev. C **11**, 426 (1975).

[58] A. J. Koning, S. Hilaire, and M. C. Duijvestijn, TALYS-1.0, in *International Conference on Nuclear Data for Science and Technology* (EDP Sciences, 2007), pp. 211–214.

[59] V. Konig and J. P. Delaroche, Study of the optical potential with polarization, Nucl. Phys. A **361**, 189 (1981).

[60] W. Dilg, W. Schantl, H. Vonach, and M. Uhl, Shell corrections in the back-shifted Fermi gas model and their effect on level densities, Nucl. Phys. A **217**, 269 (1973).

[61] J. Kopecky and M. Uhl, Test of gamma-ray strength functions in nuclear reaction model calculations, Phys. Rev. C **41**, 1941 (1990).

[62] F. Kondev, M. Wang, W. Huang, S. Naimi, and G. Audi, The NUBASE2020 evaluation of nuclear physics properties*, Chin. Phys. C **45**, 030001 (2021).

[63] J. Lippuner, R. Fernández, L. F. Roberts, F. Foucart, D. Kasen, B. D. Metzger, and C. D. Ott, Signatures of hypermassive neutron star lifetimes on r-process nucleosynthesis in the disc ejecta from neutron star mergers, Mon. Not. R. Astron. Soc. **472**, 904 (2017).

[64] S. Goriely, Uncertainties in the solar system r-abundance distribution, Astron. Astrophys. **342**, 881 (1999).

[65] S. Goriely, Radiative neutron captures by neutron-rich nuclei and the r-process nucleosynthesis, Phys. Lett. B **436**, 10 (1998).

[66] M. P. Reiter, S. Ayet San Andrés, S. Nikas, J. Lippuner, C. Andreoiu, C. Babcock, B. R. Barquest, J. Bollig, T. Brunner, T. Dickel, J. Dilling, I. Dillmann, E. Dunling, G. Gwinner, L. Graham, C. Hornung, R. Klawitter, B. Kootte, A. A. Kwiatkowski, Y. Lan *et al.*, Mass measurements of neutron-rich gallium isotopes refine production of nuclei of the first *r*-process abundance peak in neutron-star merger calculations, Phys. Rev. C **101**, 025803 (2020).